



# Highly efficient and low hysteresis methylammonium-free perovskite solar cells based on multifunctional oteracil potassium interface modification

Huan Bi <sup>a,b</sup>, Yao Guo <sup>c</sup>, Mengna Guo <sup>a</sup>, Chao Ding <sup>b</sup>, Shuzi Hayase <sup>b</sup>, Tao Mou <sup>d</sup>, Qing Shen <sup>b,\*</sup>, Gaoyi Han <sup>a,\*</sup>, Wenjing Hou <sup>a,\*</sup>

<sup>a</sup> Institute of Molecular Science, Key Laboratory of Materials for Energy Conversion and Storage of Shanxi Province, State Key Laboratory of Quantum Optics and Quantum Optics Devices, Shanxi University, Taiyuan 030006, PR China

<sup>b</sup> Faculty of Informatics and Engineering, The University of Electro-Communications, 1-5-1 Choigaoka, Chofu, Tokyo 182-8585, Japan

<sup>c</sup> School of Materials Science and Engineering, Henan Joint International Research Laboratory of Nanocomposite Sensing Materials, Anyang Institute of Technology, Anyang 455000, PR China

<sup>d</sup> Southwest Integrated Circuit Design Co., Ltd, Shapingba District, Chongqing 401332, PR China



## ARTICLE INFO

### Keywords:

Methylammonium-free  
Perovskite solar cell  
Interface engineer  
Low hysteresis  
Oteracil potassium

## ABSTRACT

Bulk and interface defects are the culprits of power conversion efficiency (PCE) loss of the perovskite solar cells (PSCs). Meanwhile, notorious hysteresis is also an obstacle on the road of the PSCs commercialization process. Consequently, it is urgently needed to develop a multifunctional modification strategy to address the above issues. Herein, we report a multifunctional buffer molecule (oteracil potassium, OP) for suppressing hysteresis and passivating defect in stable and efficient methylammonium-free PSCs ( $\text{Rb}_{0.02}(\text{FA}_{0.95}\text{Cs}_{0.05})_{0.98}\text{PbI}_{2.91}\text{Br}_{0.03}\text{Cl}_{0.06}$ ). Experimental and theoretical results prove that multi-functional OP has strong chemical interaction with  $\text{SnO}_2$  and the perovskite layer. It can not only reduce the oxygen vacancy defects in  $\text{SnO}_2$  film but also passivate the under coordinated  $\text{Pb}^{2+}$  in perovskite. At the same time, it can significantly inhibit hysteresis. Due to these beneficial effects, the PCE of the OP-modified device is over 22%, and the unencapsulated modified device exhibits more excellent humidity stability. This work provides guidance for the development of multifunctional modified molecules for high PCE, stable, and non-hysteresis PSCs.

## 1. Introduction

In the past decade, the star perovskite material has attracted researchers extensively. There is no doubt that perovskite has been widely used in various fields, such as perovskite solar cells (PSCs),<sup>[1–3]</sup> perovskite light-emitting diode,<sup>[4–6]</sup> and memristor<sup>[7,8]</sup> due to its strong light absorption, suitable bandgap, long exciton lifetime, and diffusion length.<sup>[9–11]</sup> In all of these applications, PSCs have shown amazing potential. Up to now, the certified record power conversion efficiency (PCE) of single-junction devices has achieved 25.7%.<sup>[12]</sup> Early PSCs were based on titanium dioxide ( $\text{TiO}_2$ ) electron transport layers (ETL) material. However,  $\text{TiO}_2$  is limited by its high-temperature fabrication, poor ultraviolet (UV) stability, and inability in flexible devices.<sup>[13–16]</sup> Compared with  $\text{TiO}_2$ , tin dioxide ( $\text{SnO}_2$ ) is a more suitable ETL material due to its excellent UV stability and easy fabrication process at low temperatures. It is reported that a sea of high-performance PSCs with the PCE higher than 23% are all based on  $\text{SnO}_2$  ETL.

<sup>[17–19]</sup> Even so, there are still a lot of problems that need to be solved, such as poor film crystallization, interface defects, and non-negligible hysteresis.

The PCE and stability of PSCs are closely related to the film quality of perovskite.<sup>[20–24]</sup> However, a large number of defects would be introduced in the final polycrystalline perovskite film, resulting in nonradiative recombination loss and device performance decline. A host of strategies have been developed to improve the quality of the film, such as additive engineering, substrate engineering, composition engineering, antisolvent engineering, etc.<sup>[25–31]</sup> Among these, changing the deposition substrate is one of the viable ways to improve the quality of perovskite film.<sup>[32–36]</sup> Zhang and their co-worker also got the stressed-free perovskite film by introducing a protonated amine silane coupling agent to modify the ETL and perovskite layer. So, substrate engineering is very important for obtaining high-quality perovskite films.<sup>[34]</sup>

In addition to the poor film quality, interface nonradiative

\* Corresponding authors.

E-mail addresses: [shen@pc.uec.ac.jp](mailto:shen@pc.uec.ac.jp) (Q. Shen), [han\\_gaoyi@sxu.edu.cn](mailto:han_gaoyi@sxu.edu.cn) (G. Han), [houwenjing@sxu.edu.cn](mailto:houwenjing@sxu.edu.cn) (W. Hou).

recombination caused by defects (halide vacancies, cation vacancies, and Pb-I anti-sites) can also result in device performance loss.<sup>[37]</sup> It has been well demonstrated that unfavorable  $\text{SnO}_2$ /perovskite interface contacts would lead to poor performances.<sup>[36,38,39]</sup> Bi and his co-workers employed KPF<sub>6</sub> to release the stress between ETL and perovskite layer, improve the electronic transmission capacity, and reduce the defects that exist in the interface. The results showed that both the PCE and stability of the target device were enhanced.<sup>[38]</sup> Zuo et.al used (2-carboxyethyl) dimethyl sulfonium chloride to modify the interface between  $\text{SnO}_2$  ETL and the perovskite layer.<sup>[36]</sup> It proved that both modifiers can not only passivate the defects from the surface of perovskite and  $\text{SnO}_2$  films but also reduce interfacial energy barrier via ameliorating energy band alignment. After modification, the PCE is increased from 20.72% of the control device to 22.22% of the target device. Finally, notorious hysteresis is also a stumbling block on the road of commercialization of perovskite solar cells.<sup>[40–42]</sup> Hitherto, a multitude of work has been done to reduce the interface non-

recombination and hysteresis. Our previous work has introduced the KPF<sub>6</sub> as a buffer layer to reduce the interface nonradiative recombination and hysteresis.<sup>[38]</sup> For MA-free  $\text{SnO}_2$  based perovskite solar cells, only a few works focus on both reducing both the nonradiative recombination and hysteresis. So, it is urgent to develop a multifunctional interface buffer to realize the improved crystallization morphology, and reduced interface nonradiative recombination and hysteresis.

Hither, we develop a multifunctional buffer molecule (oteracil potassium, OP) to modify the  $\text{SnO}_2$ /perovskite interface, which consists of K<sup>+</sup> and multifunctional anion simultaneously. Fourier transforms infrared (FTIR) spectroscopy proves that there is a strong chemical interaction between  $\text{SnO}_2$  and OP. Meanwhile, energy dispersive X-Ray spectroscopy (EDS) and time of flight secondary ion mass spectroscopy (ToF-SIMS) reveals that the K<sup>+</sup> exists both at the ETL/perovskite interface and inside the perovskite film. The multiple functions of OP enable the modified PSCs to provide exceptional photovoltaic performance with a PCE of 22.09% and attractive stability. The enhanced

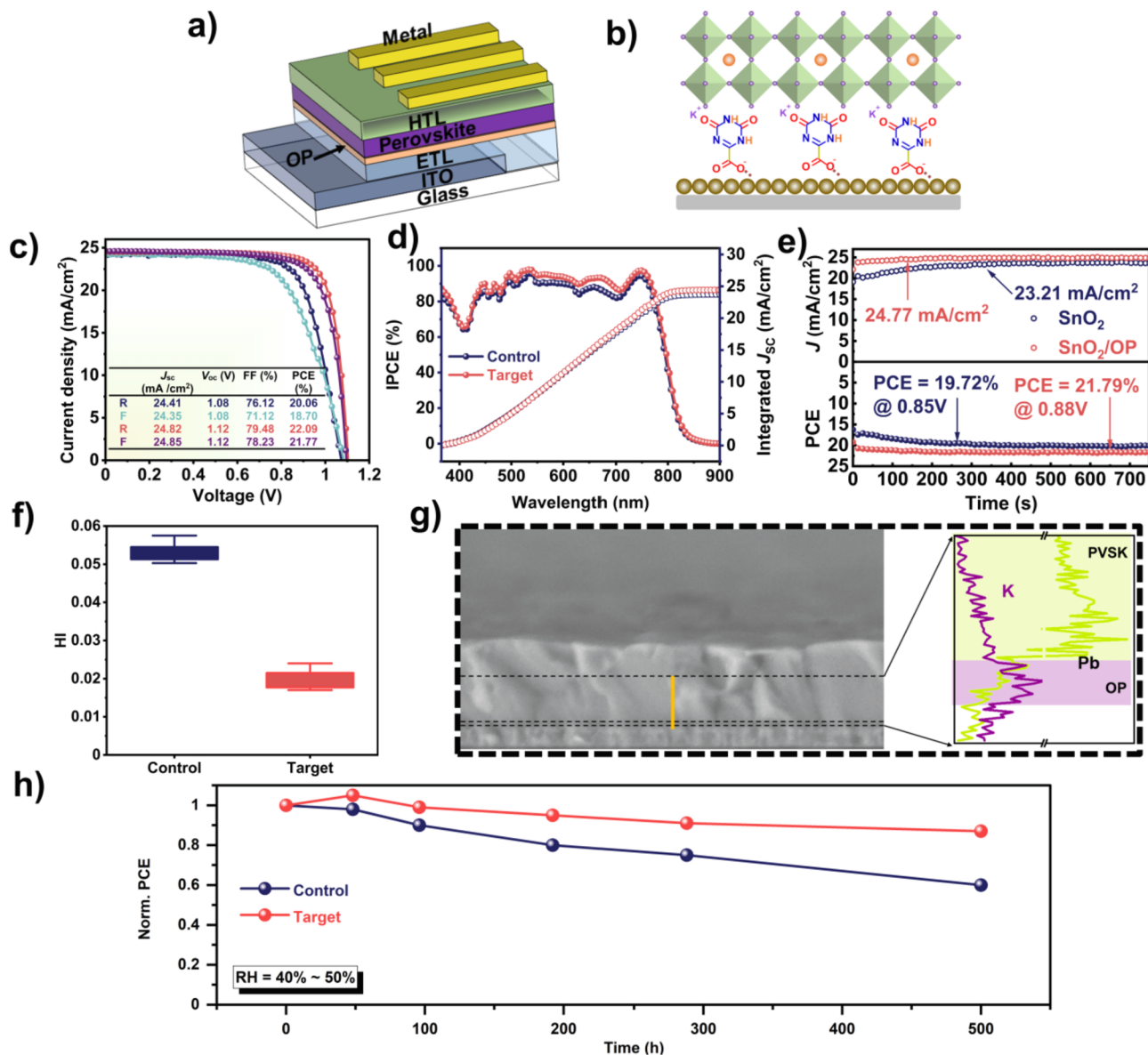


**Fig. 1.** (a) Device structure in this work. In which, OP was spin-coated on the ETL ( $\text{SnO}_2$ ). Perovskite:  $\text{Rb}_{0.02}(\text{FA}_{0.95}\text{Cs}_{0.05})_{0.98}\text{PbI}_{2.91}\text{Br}_{0.03}\text{Cl}_{0.06}$ ; (b) Schematic diagram showing the interface connection roles of OP; (c) J-V curves and (d) IPCE spectra of the champion control and target devices; (e) Continuous maximum power point tracking for the champion control and target device; (f) Statistical hysteresis index (HI) distribution; (g) Cross-section elemental liner scan based on the structure of ITO/ $\text{SnO}_2$ /OP/perovskite; (h) PCE as a function of time for the unencapsulated control and target devices aged under a relative humidity of 40–50% at room temperature in the dark.

performances can be attributed to the that our method could improve perovskite crystallization, passivate the interface defect, improve interfacial energy level alignment synchronously, and reduce hysteresis dramatically. This work highlights the critical role of multifunctional molecule strategy in realizing high PCE and stable MA-free SnO<sub>2</sub>-based perovskite solar cells.

## 2. Results and discussion

As exhibited in Fig. 1a, the device structure of ITO/SnO<sub>2</sub>/OP/perovskite/Spiro-OMeTAD/Au was used, in which, the perovskite is composed of Rb<sub>0.02</sub>(FA<sub>0.95</sub>Cs<sub>0.05</sub>)<sub>0.98</sub>PbI<sub>2.91</sub>Br<sub>0.03</sub>Cl<sub>0.06</sub>. The OP was introduced to the SnO<sub>2</sub> ETL/perovskite interface, and the corresponding schematic diagram is shown in Fig. 1b. First, the carbonyl group (C = O) can be able to passivate the halogen vacancy defects in the perovskite film. Second, the ester group (-COO) is expected to passivate the oxygen vacancy defects in the SnO<sub>2</sub> and reduce the hydroxyl groups (-OH) on the surface of SnO<sub>2</sub>.<sup>[33]</sup> Last but not least, potassium ion (K<sup>+</sup>) has been widely proved that it can both reduce the notorious hysteresis effect and improve the crystallization of the perovskite film.<sup>[38,43,44]</sup> In brief, introducing the OP as the interface layer can realize the multiple functions, which is a very attractive and urgently needed strategy.

First, the photovoltaic performances of the PSCs modified with different concentrations of OP were studied and the result was exhibited in Fig. S1 and Table S1. It was found that the PCE increased as the increased OP concentration and the target device was obtained when the concentration of OP was 0.75 mg/mL. Fig. S2 shows statistic J-V curves of control and target devices measured in reverse scan (RS) and forward scan (FS) under simulated AM 1.5G one sun illumination of 100 mW/cm<sup>2</sup>. Compared with control device with the average PCE of 19.70% ( $J_{SC} = 24.74$  mA/cm<sup>2</sup>,  $V_{OC} = 1.08$  V, FF = 73.73%), the target device shows a higher average PCE of 21.67% ( $J_{SC} = 24.88$  mA/cm<sup>2</sup>,  $V_{OC} = 1.12$  V, FF = 77.78%). Manifestly,  $V_{OC}$  and FF have a significant increase after being treated by OP. Fig. 1c and d show the J-V curves and incident photon-to-current conversion efficiency (IPCE) spectra of the devices modified without or with OP, respectively. The champion control device gave a  $J_{SC}$  of 24.41 mA/cm<sup>2</sup>, a  $V_{OC}$  of 1.08 V, an FF of 76.12%, and a PCE of 20.07%, while the target device with 0.75 mg/mL OP gave a  $J_{SC}$  of 24.82 mA/cm<sup>2</sup>, a  $V_{OC}$  of 1.12 V, an FF of 79.48%, and a PCE of 22.09%, which is very competitive (see in Supplementary Table S2). The integrated current density obtained from Fig. 1d was estimated to be 23.75 mA/cm<sup>2</sup> (control) and 24.43 mA/cm<sup>2</sup> (target), which is consistent with that obtained from J-V curves. Fig. 1e shows the stable output current density and PCE of devices with or without OP modification, respectively. Compare with the target device, the control device takes a longer time to reach a steady-state. Finally, the current density increased from 22.81 mA/cm<sup>2</sup> (control device) to 24.77 mA/cm<sup>2</sup> (target device), and PCE increased from 19.57% to 21.79%, respectively. This indicates that SnO<sub>2</sub> with OP modification can improve the stability of the device. Further, the hysteresis index (HI) of the device was established by the following equation:<sup>[33]</sup>

$$HI = (PCE_R - PCE_F)/PCE_R \quad (1)$$

where PCE<sub>R</sub> and PCE<sub>F</sub> stand for the PCE in reverse scan (R) and forward scan (F), respectively. As presented in Fig. 1f, the averaged HI was substantially reduced from 0.053 to 0.020 after OP modification. Lots of work have proved that the K<sup>+</sup> has a positive effect on reducing HI due to K<sup>+</sup> could exist in the interstitial site, after which X<sup>-</sup> anions (X: halogen atom) are bonded with K<sup>+</sup> to form immobile KX-like compounds, which can not only eliminate the mobile halide ion defects in perovskite films but also suppress the ion migration, resulting in improved stability and hysteresis-free PSCs.<sup>[38,43–47]</sup> The cross-section liner scan result of EDS and time of flight secondary ion mass spectroscopy (ToF-SIMS) were employed to verify the distribution of K<sup>+</sup>. As exhibited in Fig. 1g and S3, K<sup>+</sup> diffuses into the perovskite film, which can exist at the

boundaries and lattice of perovskite and this is consistent with previous reports.<sup>[43]</sup>

Further, we evaluated the long-term stability of unencapsulated devices under a relative humidity range of 40–50% at room temperature (Fig. 1h). As expected, after 500 h, 87% of the original efficiency can still be maintained for the target device, while the control device degrades to 60% of its beginning PCE. It hints that humidity stability increased after the SnO<sub>2</sub> is modified by OP. As shown in Fig. S4, the thermal stability is characterized by placing the devices on the hot plate in the dark air condition. After thermal aging at 60°C for 100 h, the PCE of the target device degrades to 80% of the initial PCE, whereas the PCE of the control device degrades to 40%. The above results indicate that the target device shows the improved thermal stability. The improved environmental stability can be related to the following aspects: (1) the -COO is expected to form a strong chemical interaction with Sn<sup>2+</sup> so as to reduce the oxygen defects of SnO<sub>2</sub>. (2) it is anticipated that C = O and -NH<sub>2</sub> could passivate anionic defects (e.g., undercoordinated I<sup>-</sup>, antisite PbI<sub>3</sub><sup>-</sup> and formamidinium (FA<sup>+</sup>) vacancies) and cationic defects (e.g., under-coordinated Pb) at ETL/perovskite interface. (3) OP can act as an interface chemical bridge to enhance interface contact between ETL and perovskite layer. In a word, reduced defects and improved interfacial contact both could improve the device stability.

Subsequently, FTIR (Fig. 2a) and X-ray photoelectron spectroscopy (XPS) technology (Fig. 2b-c) were adopted to characterize the chemical interactions between SnO<sub>2</sub> and OP or between OP and perovskite clearly. As displayed in Fig. 2a, after modifying the OP on SnO<sub>2</sub>, the characteristic peak of O-Sn-O shifted from 791 cm<sup>-1</sup> to a higher wave-number (798 cm<sup>-1</sup>), and the stretching vibration peak of C-O shifted from 1234 cm<sup>-1</sup> to 1249 cm<sup>-1</sup>. This can be attributed to the strong chemical interaction between -COO in OP and Sn in SnO<sub>2</sub>. On the other hand, as shown in Fig. S5a, after OP modification, the binding energy of Sn 3d<sub>5/2</sub> (486.2 eV) and 3d<sub>3/2</sub> (494.5 eV) for bare SnO<sub>2</sub> film decreased to 485.7 eV and 494.3 eV, which proved that a strong chemical interaction exists between SnO<sub>2</sub> and OP. Further, the binding energy of Pb 4f showed a similar trend after introducing OP, which confirms the existence of the strong chemical interaction between OP and perovskite (Fig. S5b). As revealed by O 1 s spectra in Fig. 2b-c, an asymmetric broad peak appeared for both bare SnO<sub>2</sub> and OP-treated SnO<sub>2</sub> films, which can be deconvoluted into two peaks of ~ 530 eV and ~ 531 eV, which is assigned to the lattice oxygen and the chemisorbed oxygen atoms or hydroxyl groups, respectively.<sup>[39]</sup> The result showed that after modifying, the intensity of the lattice oxygen reduced and the intensity of adsorbed oxygen increased, which proved that -COO is connected to the SnO<sub>2</sub>. In one nutshell, both FTIR and XPS results confirmed that the OP can act as the double-connected interfacial chemical bridge to link the SnO<sub>2</sub>/perovskite interface. Double-connected structures like this conduct to facilitate interfacial charge transfer.

The UV-vis absorption spectra and X-ray diffraction (XRD) were employed to investigate the effect of OP on the light absorption and crystallinity of the perovskite films. As presented in Fig. 2d, a slightly improved UV-vis absorption intensity was shown for the target film. As displayed in Fig. 2e, perovskite film has the same structure whether OP modified or not. However, the perovskite film based on OP-treated SnO<sub>2</sub> shows a higher crystallization intensity than the control film.

The scanning electron microscopy (SEM) is employed to study the effect of OP on the morphology of the perovskite film intuitively. As shown in Fig. 3a and b, we can see that after OP modification, pinholes were reduced obviously. Meanwhile, as presented in the illustration, the average grain size increased from 500 nm (control film) to 680 nm (target film) significantly. Besides, the grain size distribution becomes more uniform, which can be inferred from the standard deviation. The increased crystal size and the decreased pinholes can be attributed to the change of the substrates and K<sup>+</sup> regulates film growth.<sup>[48–52]</sup> Improved light-harvesting efficiency and crystallization were responsible for the slightly increased  $J_{SC}$  and IPCE.

Photoluminescence (PL) spectra and time-resolved photo-

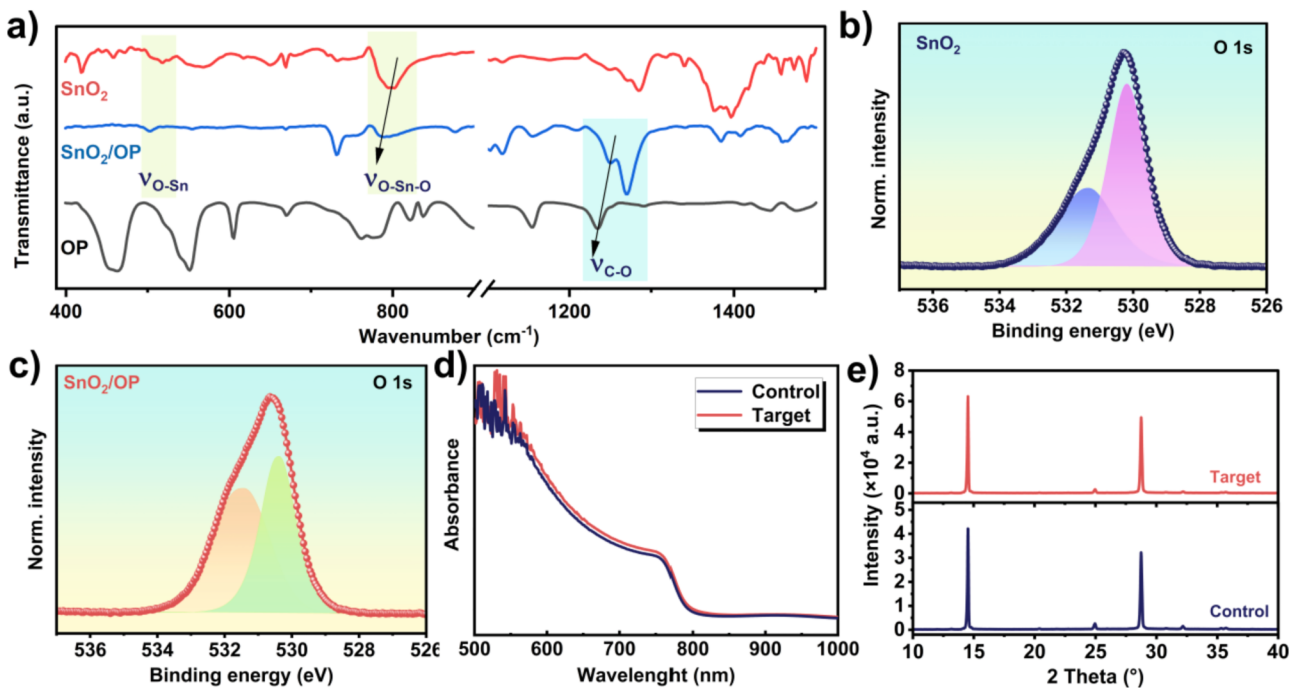


**Fig. 2.** FTIR spectra of (a) SnO<sub>2</sub>/OP, SnO<sub>2</sub>, and OP; High-resolution XPS spectra of O 1 s in (b) SnO<sub>2</sub> and (c) SnO<sub>2</sub>/OP films; (d) UV–Vis absorption spectra and (e) XRD patterns of the perovskite film modified without or with OP.

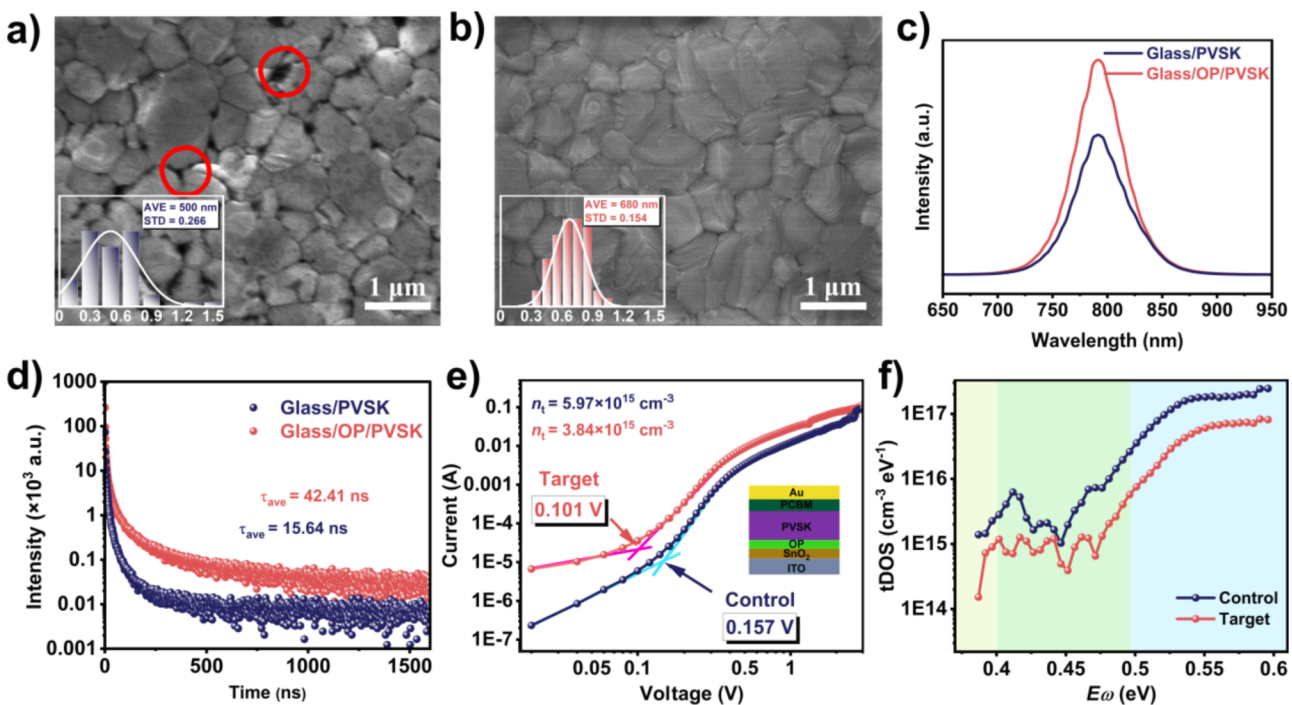


**Fig. 3.** SEM image of (a) bare perovskite film and (b) target perovskite film with the illustration of crystal size statistics (the illustration shows the crystals size statistics, unit:  $\mu\text{m}$ ); (c) PL and (d) TRPL of the perovskite film with the structure of Glass/perovskite and Glass/OP/perovskite; (e) Dark J–V curves with the structures of ITO/SnO<sub>2</sub>/perovskite/PCBM/Ag and ITO/SnO<sub>2</sub>/OP/perovskite/PCBM/Ag. (f) tDOS of the two types of devices, as measured by the TAS method.

luminescence (TRPL) kinetics of the perovskite films with the structure of Glass/perovskite and Glass/OP/perovskite are used to characterize the effect of the OP modification on the film defects and carrier non-radiative recombination in the perovskite. As illustrated in Fig. 3c, the intensity of the PL increased significantly after introducing OP into the SnO<sub>2</sub>/perovskite interface. TRPL curves were displayed in Fig. 3d and can be fitted well by the double-exponential:[36].

$$I(t) = A_1 e^{(-t/\tau_1)} + A_2 e^{(-t/\tau_2)} \quad (2)$$

where  $\tau_1$  is the fast decay time and  $\tau_2$  stands for the slow decay time,  $A_1$  and  $A_2$  are the amplitude of the fast and slow decay process, respectively. The average photoexcited carrier lifetime ( $\tau_{\text{ave}}$ ) can be obtained by the equation of:

$$\tau_{ave} = \frac{A_1\tau_1^2 + A_2\tau_2^2}{A_1\tau_1 + A_2\tau_2} \quad (3)$$

and the corresponding fitting parameters presented in Table S3.[36] It can be seen clearly that the perovskite film based on the OP-treated  $\text{SnO}_2$  has a longer average photoexcited carrier lifetime (42.41 ns) than bare perovskite film (18.92 ns), which indicated the defects of the perovskite films decreased after  $\text{SnO}_2$  was treated by OP. Then, we use the space charge limited current (SCLC) measurement to uncover the defect densities of perovskite films with the structure of ITO/ $\text{SnO}_2$ /(OP)/perovskite/PCBM/Ag. As shown in Fig. 3e, after treating by OP, the trap-filled limit voltage ( $V_{TFL}$ ) decreases from the original 0.157 V to 0.101 V. Generally, the trap density of the film ( $n_t$ ) can be established by the equation of:[53]

$$n_t = \frac{2\varepsilon_0 e V_{TFL}}{eL^2} \quad (4)$$

where  $\varepsilon$  is the dielectric constant of the perovskite,  $\varepsilon_0$  is the vacuum dielectric constant,  $e$  is the elementary charge, and  $L$  is the thickness film of the perovskite.[54] The calculated defect density of the target film is  $3.84 \times 10^{15} \text{ cm}^{-3}$ , lower than that of the control film ( $5.97 \times 10^{15} \text{ cm}^{-3}$ ). Thermal admittance spectroscopy (TAS) measurements were conducted to further analyze the trap density of states (tDOS) in energy space for the control and target devices.[55] As shown in Fig. 3f, there are three typical trap state bands, e.g.,  $E\omega < 0.40 \text{ eV}$  (band I),  $0.40 \text{ eV} < E\omega < 0.50 \text{ eV}$  (band II), and  $E\omega > 0.50 \text{ eV}$  (band III), among which the deep trap depth regions (band II and III) are mainly related to the surface defects, and the shallower trap-states (band I) are more closely related to the bulk or grain boundaries of perovskite.[55] After being modified by OP, three bands have all been reduced, especially for the band II and III, indicating that both shallow level defects and deep level defects can be passivated, especially for the deep level defects. In a word, after

introducing the buffer layer (OP), the defect density of the film reduced, which can be attributed to the improved crystallinity of the perovskite film and effective defects passivation roles of C = O, N-H, and K<sup>+</sup> in OP molecules, such as undercoordinated Pb. And thus, the Shockley–Read–Hall nonradiative recombination was suppressed, which is another reason for the improvement of  $V_{OC}$  and FF. In addition, increased grain size can also explain the improved  $V_{OC}$  and FF partially.

However, this does not mean that the reduced defect is the sole reason for the improved  $V_{OC}$  and FF. In order to get insights into the origin of improved  $V_{OC}$  and FF from the electronic dynamics, PL and TRPL measurements were carried out with the structure of ITO/ $\text{SnO}_2$ /(OP)/perovskite. As presented in Fig. 4a, after OP modification, the PL intensity decreased and the averaged photoexcited carrier lifetime decreased from the original 7.39 ns to 4.78 ns (Fig. 4b, Table S4), which indicates that the electron can be better extracted after OP modification. Then, Mott–Schottky curves were employed to reveal the change of the built-potentials ( $V_{bi}$ ), which is the driving force of electron transport at the interface. As shown in Fig. S6, the  $V_{bi}$  of the control and target device are 0.96 V and 1.01 V, respectively. The improved  $V_{bi}$  after the introduction of OP encourages us to uncover the deep reason for the electron transfer and recombination through light-intensity-dependent  $V_{OC}$  curves as shown in Fig. 4c. The ideality factor ( $n$ ) can be used to evaluate the charge recombination. The  $n$  is obtained by a slope of  $k_B T/q$  of light-dependent  $V_{OC}$ , where  $k_B$ ,  $T$ , and  $q$  are the Boltzmann's constant, Kelvin temperature, and element charge, respectively. The  $n = 1$  indicates a trap-free condition, while the  $n$  over 1 suggests the existence of defect-induced non-radiative recombination.[56] The  $n$  was reduced from 2.18 of the control devices to 1.63 of the target devices, confirming that the trap-assisted non-radiative recombination was restrained observably. Ultraviolet photoelectron spectroscopy (UPS) measurement was used to elucidate the influence of the OP on the surface energy levels of the  $\text{SnO}_2$  (Fig. 4d and Fig. S7–9) ETL. Conduction band minimum

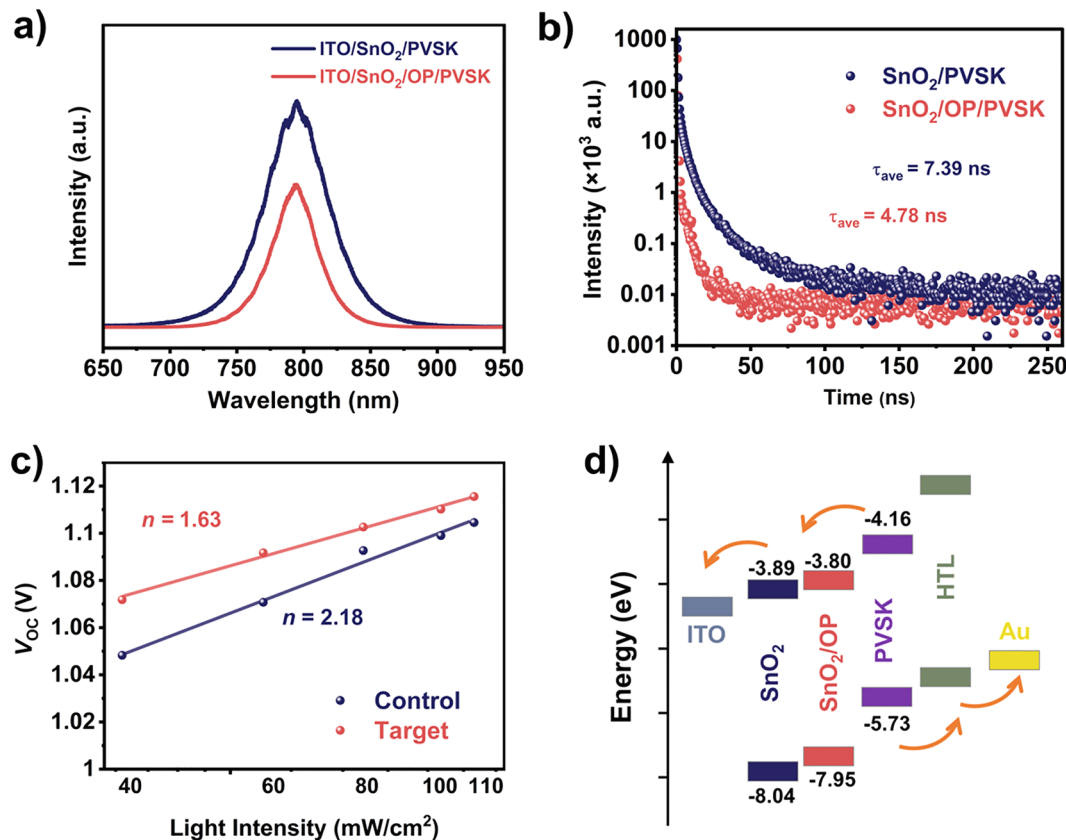


**Fig. 4.** (a) PL and (b) TRPL of the perovskite film with the structure of ITO/ $\text{SnO}_2$ /perovskite and ITO/ $\text{SnO}_2$ /OP/perovskite; (c)  $V_{OC}$  versus light intensity for the control and target devices; (d) Energy-level scheme for the control and target perovskite films.

(CBM) and valence band maximum (VBM) are calculated according to the previous work.[33] The energy levels of the control and target devices are shown in Fig. 4d. The CBM (-3.80 eV) and VBM (-7.95 eV) of the SnO<sub>2</sub> thin film with OP modified were slightly higher than bare SnO<sub>2</sub> film (CBM: -3.89 eV and VBM: -8.04 eV), resulting in a more matchable energy level, which can improve the  $V_{OC}$ .[55] Meanwhile, a suitable energy level can also reduce the charge accumulation at the interface, which is another main reason for inhibited hysteresis. In a word, improved electron transport is also the main reason for increased  $V_{OC}$  and FF.[54,57].

The first principle calculation was further employed to uncover the strong chemical interaction between SnO<sub>2</sub> and OP. We can see that after introducing the oxygen vacancy, the whole system is in a more stable state due to the energy shifted to lower energy in Fig. 5a. Meanwhile, the s and p orbitals of the Sn and OP show a lot of overlap (Fig. 5b), which indicated that there is a strong chemical interaction between Sn and OP, which is consistent with the results of FTIR and XPS. The charge density difference (CDD) makes the chemical interaction between Sn and OP more obvious. As displayed in Fig. 5c and d, -COO occupies the oxygen position of SnO<sub>2</sub> thin film. Due to the existence of lone electron pairs of the O in -COO, which can form a strong chemical interaction between -COO and Sn, then, the oxygen vacancy in SnO<sub>2</sub> could effectively be reduced, which is highly consistent with the results of XPS and FTIR. Further, the chemical interaction between OP and perovskite also was evaluated by CDD and shown in Fig. 5e and f. Here, we constructed a perovskite cell containing halogen (I) vacancy to evaluate the effect of OP on halogen vacancy. As exhibited in Fig. 5e, an apparent charge vacancy exists between adjacent Pb<sup>2+</sup>. After OP was introduced, the strong chemical interaction forms between C = O and under coordinated Pb<sup>2+</sup> due to the charge density has changed significantly whether OP or Pb, which proves that a chemical interaction was formed between OP and perovskite film and consistent with the result of FTIR and XPS. In addition, CDD also reveals a strong chemical relationship between -NH and FA<sup>+</sup> (Fig. S10). The theoretical results proved the positive role of OP

in PSCs once again.

### 3. Conclusions

In summary, we have developed a multifunctional interface modification strategy, where OP possessing simultaneously C = O and K<sup>+</sup> is employed to manage the SnO<sub>2</sub>/perovskite interface. OP can both passivate the defects and reduce the hysteresis. FTIR and XPS results proved that a strong chemical relationship between whether SnO<sub>2</sub> and OP or OP and perovskite film, which can not only reduce oxygen vacancies in SnO<sub>2</sub> films but also can reduce the defects in perovskite films. Theoretical results further revealed the strong chemical interaction between SnO<sub>2</sub> and OP. Finally, the target device exhibited a high PCE of 22.09% and good humidity stability. Also, disreputable hysteresis is reduced significantly. This work guides the realization of high PCE, stable and low hysteresis perovskite solar cells using cation and anion regulation.

## 4. Experimental section

### 4.1. Materials

Thermo Scientific (tin (IV) oxide, 15% in H<sub>2</sub>O colloidal dispersion) provided the SnO<sub>2</sub> colloid precursor. Macklin provided oteracil potassium (OP) and acetonitrile (ACN, 99.8%). Xi'an Polymer Light Technology Corp. supplied lead (II) iodide (PbI<sub>2</sub>, 99.99 percent), lead (II) chloride (PbCl<sub>2</sub>, 99.99%), and methylamine hydrochloride (MACl, 99.5%). Advanced Electron Technology CO., Ltd. supplied Lead (II) bromide (PbBr<sub>2</sub>, 99.9%), Formamidine hydroiodide (FAI, 99.9%), bis (trifluoromethane) sulfonimide lithium salt (Li-TFSI, 99%), 2,2',7,7'-Tetrakis[N,N-di(4-methoxyphenyl)amino]-9,9'-spirobifluorene (Spiro-OMeTAD, 99.86%) and 4-*tert*-butyl pyridine (*t*BP, 99%). Sigma Aldrich provided N,N-dimethylformamide (DMF, 99.8 percent), dimethyl sulfoxide (DMSO, 99.9 percent), and chlorobenzene (CB, 99.8 percent). All

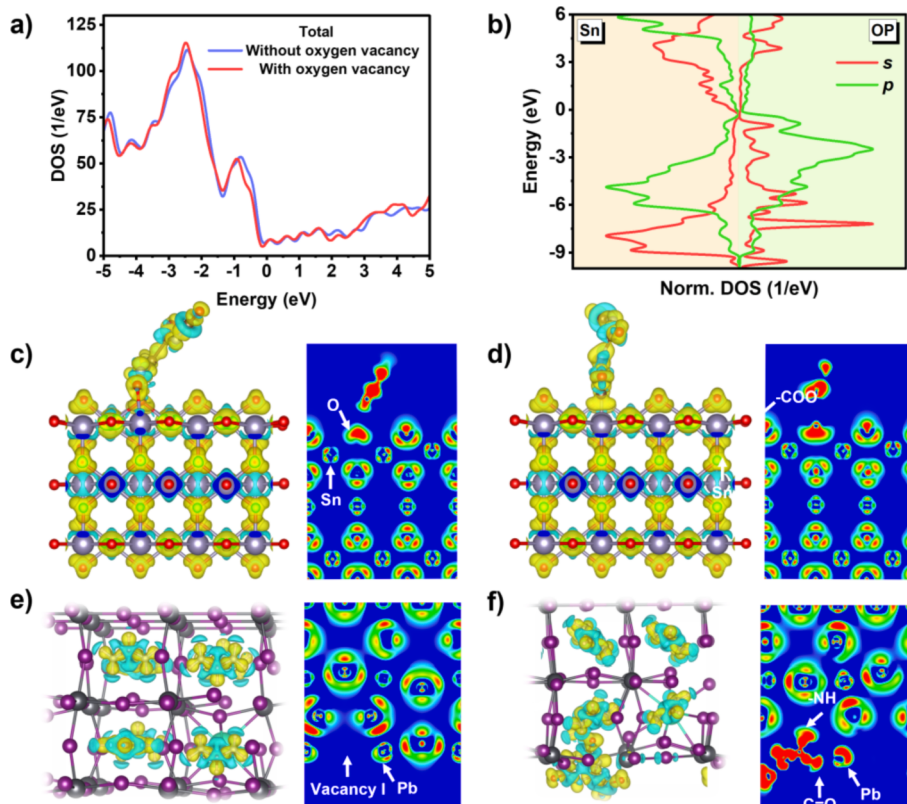


**Fig. 5.** (a) Total DOS without or with oxygen vacancy with the structure of SnO<sub>2</sub>/OP; (b) The DOS of s and p orbitals of the surface-Sn (SnO<sub>2</sub>) and OP with the structure of SnO<sub>2</sub>/OP; The charge density difference of SnO<sub>2</sub>/OP structure without (c) or with (d) oxygen vacancy and the distribution of the corresponding (010) plane section charge density difference with isosurface value of 0.017 e/Å<sup>3</sup>. The charge density difference of I vacancy without (e) or with (f) OP modification and the distribution of the corresponding (010) plane section charge density difference with isosurface value of 0.004 e/Å<sup>3</sup>.

chemical reagents were utilized just as they were received, with no additional purification.

#### 4.2. Device fabrication

ITO glasses (bought from Jiangsu Yanchang Sunlaite New Energy Co., Ltd. for  $7 \sim 9 \Omega$  per square) were ultrasonically cleaned for 20 min in sequence with detergent water and ethanol. After being blown dry by nitrogen (99.99%), and then the ITO was treated for 30 min with ultraviolet ozone (UV-O3). The  $\text{SnO}_2$  colloidal solution was prepared by combining the  $\text{SnO}_2$  solution with deionized water at a volume ratio of 1:3. Diluted  $\text{SnO}_2$  colloidal solution was spin-coated on ITO substrates for 30 s at a speed of 3000 rpm, and the  $\text{SnO}_2$  film was annealed at 150 °C for 30 min. After cooling to ambient temperature, it was subjected to a 20-minute UV-O3 treatment. The substrates were then placed in an argon-filled glovebox for perovskite deposition. Different mass concentrations of OP (0, 0.35, 0.75, and 1 mg/mL) were dissolved in water for OP treatment, and then 20  $\mu\text{L}$  of OP were spin-coated onto the  $\text{SnO}_2$  film for 30 s at 5000 rpm. Perovskite ( $\text{Rb}_{0.02}(\text{FA}_{0.95}\text{Cs}_{0.05})_{0.98}\text{PbI}_{2.91}\text{Br}_{0.03}\text{Cl}_{0.06}$ ) precursor solution was prepared by dissolving  $\text{PbI}_2$  (1.48 M),  $\text{PbBr}_2$  (0.023 M),  $\text{RbI}$  (0.03 M),  $\text{PbCl}_2$  (0.045 M),  $\text{CsI}$  (0.76 M), FAI (1.45 M) and  $\text{MACl}$  (0.52 M) into the DMSO/DMF (1/4, v/v) mixture. The perovskite film was deposited using a sequential spin-coating method at 4000 rpm for 30 s, with 80  $\mu\text{L}$  of CB antisolvent dripped over perovskite films for 16 s before the program was terminated, and the film was subsequently annealed at 130 °C for 30 min. 72.3 mg Spiro-OMeTAD, 28.8  $\mu\text{L}$  4-*tert*-butyl pyridine (tBP), and 17.5  $\mu\text{L}$  lithium bis(trifluoromethane sulfonyl)imide (Li-TFSI) stock solution (520 mg Li-TFSI in 1 mL acetonitrile) in 1 mL CB were combined to make the Spiro-OMeTAD solution. The hole transport layer was then formed by spin-coating 20  $\mu\text{L}$  of Spiro-OMeTAD solution onto the perovskite films at 4000 rpm for 33 s. Finally, about 100 nm metal counter electrode was thermally evaporated on the top of Spiro-OMeTAD film under a vacuum of  $3 \times 10^{-3}$  Pa through using a shadow mask.

#### 4.3. Characterization

The metal mask was used to determine the effective active area of the device to be 0.1 cm<sup>2</sup>, and *J-V* curves were generated using a solar simulator and a Keithley 2400 source meter. An FTIR spectrometer was used to acquire Fourier transformed infrared (FTIR) spectra (Tensor27, BRUKER, Germany). An Agilent 8453 UV-Vis G1103A spectrometer was used to measure UV-Vis spectra. A Confocal Raman system (iHR 550 HORIBA) with a 532 nm laser was used to record steady-state photoluminescence (PL). Thermo Avantage (v5.9921) software was used to analyze and interpret XPS spectra acquired from a Physical Electronics Model 5700 XPS equipment. SEM observations were carried out in ADD mode on SEM (FESEM, JEOL-JSM-6701F). An X-ray diffractometer (XRD, BRUKER, Germany). The PHI 5000 VersaProbe III was used to perform ultraviolet photoelectron spectroscopy (UPS) using a He I source (21.22 eV) and a negative bias of 9.0 V. On a field emission scanning electron microscope (JEM-7900F, Japan) equipped with EDS equipment, the energy-dispersive X-ray spectroscopy (EDS) measurement was performed. In Shanxi University's State Key Laboratory of Quantum Optics and Quantum Optics Devices, time-resolved photoluminescence (TRPL) was measured using a self-built scanning confocal system based on an inverted microscope (Nikon, TE2000-U) with a 450 nm laser. An electrochemical workstation was used to perform thermal admittance spectroscopy (TAS) experiments (CHI 660e). Time-of-flight secondary ion mass spectrometry (ToF-SIMS) measurement was carried out using a dual-beam TOF-SIMS IV (IONTOF) spectrometer equipped with a 30 keV, 1 pA  $\text{Bi}_3^+$  beam for the analysis and a 1 keV, 1 nA  $\text{O}^{2-}$  ion beam for the sputtering operated in noninterlaced mode.

#### 4.4. Computational details and models

All density functional theory (DFT) calculations were performed using the Vienna *ab initio* Simulation Package (VASP).<sup>[58,59]</sup> The augmented plane wave (PAW) method<sup>[60]</sup> was used to describe the electron-ion interactions. The generalized gradient approximation (GGA) with the Perdew-Burke- Ernzerhof parameterization (PBE)<sup>[61]</sup> was applied to handle the exchange and correlation functionals. The plane wave cut-off energy was set to be 400 eV. The Gaussian smearing method<sup>[62]</sup> with 0.1 eV width was employed to determine the electron occupancy. The k-point interval distribution of Monkhorst-Pack<sup>[63]</sup> was 0.2 Å<sup>-1</sup> for structural optimization. Vacuum space of 20 Å was employed in the z direction to avoid any spurious interaction. Spurious dipole interactions between periodic images were corrected by the dipole correction (IDIPOL = 3). To consider the van der Waals interaction, the long-range dispersion forces are accounted for using the Grimme DFT-D3 method.<sup>[64]</sup> The break conditions for the electronic self-consistent loop and the ionic relaxation loop were set at  $1.0 \times 10^{-6}$  eV and 0.005 eV/Å, respectively. The initial crystal structure corresponds to the rutile type tetragonal crystal structure of  $\text{SnO}_2$  (space group: P42/mnm). To model the (110) surface, a 3 × 2 supercell with 108 atomic sites was employed to investigate the adsorption. The oxygen terminated (110) surface was selected in work because it is generally considered to be the most stable one.<sup>[65]</sup> The crystal structures, charge density difference isosurfaces, and contour plots were generated by the VESTA program.<sup>[66]</sup>

#### Declaration of Competing Interest

The authors declare that they have no known competing financial interests or personal relationships that could have appeared to influence the work reported in this paper.

#### Acknowledgements

This work was financially supported by the National Natural Science of China (U21A20172, 61804091, and U21A6004), Scientific and Technological Innovation Programs of Higher Education Institutions in Shanxi (2020L0002), and the Natural Science of Shanxi Province under Grant (201901D211127), Program of State Key Laboratory of Quantum Optics and Quantum Optics Devices (No: KF201910). we are grateful for the Scientific Research Start-up Funds of Shanxi University, and Hundred Talents Plan of Shanxi Province. This research was partly supported by the Japan Science and Technology Agency (JST) Mirai program (JPMJMI17EA). We also would like to thank Shiyanjia Lab (www.shiyanjia.com) for the support of XPS and UPS tests.

#### Appendix A. Supplementary data

Supplementary data to this article can be found online at <https://doi.org/10.1016/j.cej.2022.135671>.

#### References

- [1] S.-H. Turren-Cruz, A. Hagfeldt, M. Saliba, Methylammonium-free, high-performance, and stable perovskite solar cells on a planar architecture, *Science* 362 (6413) (2018) 449–453.
- [2] M. Mateen, Z. Arain, Y.I. Yang, X. Liu, S. Ma, C. Liu, Y. Ding, X. Ding, M. Cai, S. Dai, MACl-Induced intermediate engineering for high-performance mixed-cation perovskite solar cells, *ACS Appl. Mater. Interfaces* 12 (9) (2020) 10535–10543.
- [3] X. Zhu, S. Yang, Y. Cao, L. Duan, M. Du, J. Feng, Y. Jiao, X. Jiang, Y. Sun, H. Wang, S. Zuo, Y. Liu, S. Liu, Ionic-liquid-perovskite capping layer for stable 24.33%-efficient solar cell, *Adv. Energy Mater.* 12 (2022) 2103491.
- [4] M. Karlsson, Z. Yi, S. Reichert, X. Luo, W. Lin, Z. Zhang, C. Bao, R. Zhang, S. Bai, G. Zheng, P. Teng, L. Duan, Y. Lu, K. Zheng, T. Pullerits, C. Deibel, W. Xu, R. Friend, F. Gao, Mixed halide perovskites for spectrally stable and high-efficiency blue light-emitting diodes, *Nat. Commun.* 12 (2021) 361.

- [5] C. Zou, C. Zhang, Y.-H. Kim, L.Y. Lin, J.M. Luther, The path to enlightenment: progress and opportunities in high efficiency halide perovskite light-emitting devices, *ACS Photonics* 8 (2021) 386–404.
- [6] M. Liu, Q. Wan, H. Wang, F. Carulli, X. Sun, W. Zheng, L. Kong, Q. Zhang, C. Zhang, Q. Zhang, S. Brovelli, L. Li, Suppression of temperature quenching in perovskite nanocrystals for efficient and thermally stable light-emitting diodes, *Nat. Photonics* 15 (2021) 379–U62.
- [7] Z. Xiao, J. Huang, Energy-efficient hybrid perovskite memristors and synaptic devices, *Adv. Electron. Mater.* 2 (2016) 1600100.
- [8] Y. Fang, S. Zhai, L. Chu, J. Zhong, Advances in halide perovskite memristor from lead-based to lead-free materials, *ACS Appl. Mater.* 13 (15) (2021) 17141–17157.
- [9] K. Maas, E. Villepreux, D. Cooper, E. Salas-Colera, J. Rubio-Zuazo, G.R. Castro, O. Renault, C. Jimenez, H. Roussel, X. Mescot, Q. Rafhay, M. Boudard, M. Burriel, Tuning memristivity by varying the oxygen content in a mixed ionic-electronic conductor, *Adv. Funct. Mater.* 30 (2020) 1909942.
- [10] D. Li, Y. Huang, G. Wang, Q. Lian, R. Shi, L. Zhang, X. Wang, F. Gao, W. Kong, B. Xu, C. Cheng, S. Li, Boosting the performance of MA-free inverted perovskite solar cells via multifunctional ion liquid, *J. Mater. Chem. A* 9 (21) (2021) 12746–12754.
- [11] X.-X. Gao, W. Luo, Y.I. Zhang, R. Hu, B. Zhang, A. Züttel, Y. Feng, M. K. Nazeeruddin, Stable and high-efficiency methylammonium-free perovskite solar cells, *Adv. Mater.* 32 (9) (2020) 1905502.
- [12] NREL, 2021. <https://www.nrel.gov/pv/cell-efficiency.html>.
- [13] Y. Mei, H. Liu, X. Li, S. Wang, Hollow TiO<sub>2</sub> spheres as mesoporous layer for better efficiency and stability of perovskite solar cells, *J. Alloys Compd.* 866 (2021), 158079.
- [14] H. Sun, D. Xie, Z. Song, C. Liang, L. Xu, X. Qu, Y. Yao, D. Li, H. Zhai, K. Zheng, C. Cui, Y. Zhao, Interface defects passivation and conductivity improvement in planar perovskite solar cells using Na<sub>2</sub>S-Doped compact TiO<sub>2</sub> electron transport layers, *ACS Appl. Mater.* 12 (20) (2020) 22853–22861.
- [15] H.-Y. Yang, A. Chuquer, S.-H. Han, G.S. Gaudel, X.-H. Pham, H.-M. Kim, W.-J. Yun, B.-H. Jun, W.-Y. Rho, Optimizing the aspect ratio of nanopatterned mesoporous TiO<sub>2</sub> thin-film layer to improve energy conversion efficiency of perovskite solar cells, *Int. J. Mol. Sci.* 22 (2021) 12235.
- [16] G. Yin, G. Liu, L. Ke, M. Rong, H. Li, N-doped anatase TiO<sub>2</sub> as an efficient electron transport layer for mesoporous perovskite solar cells, *Applied Physics Express* 14 (2021), 076503.
- [17] E.H. Jung, B. Chen, K. Bertens, M. Vafaei, S. Teale, A. Proppe, Y.i. Hou, T. Zhu, C. Zheng, E.H. Sargent, Bifunctional surface engineering on SnO<sub>2</sub> reduces energy loss in perovskite solar cells, *ACS Energy Lett.* 5 (9) (2020) 2796–2801.
- [18] Y. Guo, H. Lei, C. Wang, J. Ma, C. Chen, X. Zheng, G. Yang, L. Xiong, Z. Tan, Reconfiguration of interfacial and bulk energy band structure for high-performance organic and thermal-stability enhanced perovskite solar cells, *Sol. RRL* 4 (2020) 1900482.
- [19] J. Zhuang, P. Mao, Y. Luan, X. Yi, Z. Tu, Y. Zhang, Y. Yi, Y. Wei, N. Chen, T. Lin, F. Wang, C. Li, J. Wang, Interfacial passivation for perovskite solar cells: the effects of the functional group in phenethylammonium iodide, *ACS Energy Lett.* 4 (2019) 2913–2921.
- [20] F. Zhang, K. Zhu, Additive engineering for efficient and stable perovskite solar cells, *Adv. Energy Mater.* 10 (2019) 1902579.
- [21] S. Liu, Y. Guan, Y. Sheng, Y. Hu, Y. Rong, A. Mei, H. Han, A review on additives for halide perovskite solar cells, *Adv. Energy Mater.* 10 (2020) 345–351.
- [22] K. Liu, Q. Liang, M. Qin, D. Shen, H. Yin, Z. Ren, Y. Zhang, H. Zhang, P.W.K. Fong, Z. Wu, J. Huang, J. Hao, Z. Zheng, S.K. So, C.-S. Lee, X. Lu, G. Li, Zwitterionic-surfactant-assisted room-temperature coating of efficient perovskite solar cells, *Joule* 4 (11) (2020) 2404–2425.
- [23] Y.i. Yang, C. Liu, A. Mahata, M.o. Li, C. Roldán-Carmona, Y. Ding, Z. Arain, W. Xu, Y. Yang, P.A. Schouwink, A. Züttel, F. De Angelis, S. Dai, M.K. Nazeeruddin, Universal approach toward high-efficiency two-dimensional perovskite solar cells via a vertical-rotation process, *Energy Environ. Sci.* 13 (9) (2020) 3093–3101.
- [24] D. Li, W. Kong, H. Zhang, D. Wang, W. Li, C. Liu, H. Chen, W. Song, F. Gao, A. Amini, B. Xu, S. Li, C. Cheng, Bifunctional ultrathin PCBM enables passivated trap states and cascaded energy level toward efficient inverted perovskite solar cells, *ACS Appl. Mater.* 12 (17) (2020) 20103–20109.
- [25] Y. Zhao, P. Zhu, M. Wang, S. Huang, Z. Zhao, S. Tan, T.-H. Han, J.-W. Lee, T. Huang, R. Wang, J. Xue, D. Meng, Y.u. Huang, J. Marian, J. Zhu, Y. Yang, A polymerization-assisted grain growth strategy for efficient and stable perovskite solar cells, *Adv. Mater.* 32 (17) (2020) 1907769.
- [26] B. Yu, L. Zhang, J. Wu, K. Liu, H. Wu, J. Shi, Y. Luo, D. Li, Z. Bo, Q. Meng, Application of a new  $\pi$ -conjugated ladder-like polymer in enhancing the stability and efficiency of perovskite solar cells, *J. Mater. Chem. A* 8 (3) (2020) 1417–1424.
- [27] Y. Yang, T. Chen, D. Pan, J. Gao, C. Zhu, F. Lin, C. Zhou, Q. Tai, S. Xiao, Y. Yuan, Q. Dai, Y. Han, H. Xie, X. Guo, MAPbI<sub>3</sub>/agarose photoactive composite for highly stable unencapsulated perovskite solar cells in humid environment, *Nano Energy* 67 (2020), 104246.
- [28] D. Wang, L. Huang, Q. Chen, L. Hu, F. Zeng, X. Zhou, L. Zhang, C. Liu, X. Wang, L. Yan, B. Xu, A dual function-enabled novel zwitterion to stabilize a Pb-I framework and passivate defects for highly efficient inverted planar perovskite solar cells, *Chem. Commun.* 56 (51) (2020) 6929–6932.
- [29] R. Tao, W. Fang, F. Li, Z. Sun, L. Xu, Lanthanide-containing polyoxometalate as luminescent down-conversion material for improved printable perovskite solar cells, *J. Alloys Compd.* 823 (2020), 153738.
- [30] J.V. Patil, S.S. Mali, C.K. Hong, Efficient and stable all-inorganic niobium-incorporated CsPbI<sub>2</sub>Br-based perovskite solar cells, *ACS Appl. Mater.* 12 (24) (2020) 27176–27183.
- [31] H. Bian, H. Wang, Z. Li, F. Zhou, Y. Xu, H. Zhang, Q. Wang, L. Ding, S.F. Liu, Z. Jin, Unveiling the effects of hydrolysis-derived DMAI/DMAPbI<sub>x</sub> intermediate compound on the performance of CsPbI<sub>3</sub> solar cells, *Adv. Sci. J.* 7 (2020) 1902868.
- [32] S. You, H. Zeng, Z. Ku, X. Wang, Z. Wang, Y. Rong, Y. Zhao, X. Zheng, L. Luo, L. Li, S. Zhang, M. Li, X. Gao, X. Li, Multifunctional polymer-regulated SnO<sub>2</sub> nanocrystals enhance interface contact for efficient and stable planar perovskite solar cells, *Adv. Mater.* 32 (43) (2020) 2003990.
- [33] J. Chen, X. Zhao, S.G. Kim, N.G. Park, Multifunctional chemical linker imidazoleacetic acid hydrochloride for 21% efficient and stable planar perovskite solar cells, *Adv. Mater.* 31 (2019) 1902902.
- [34] C.-C. Zhang, S. Yuan, Y.-H. Lou, Q.-W. Liu, M. Li, H. Okada, Z.-K. Wang, Perovskite films with reduced interfacial strains via a molecular-level flexible interlayer for photovoltaic application, *Adv. Mater.* 32 (38) (2020) 2001479.
- [35] Q. Zhou, J. Duan, X. Yang, Y. Duan, Q. Tang, Interfacial strain release from the WS<sub>2</sub>/CsPbBr<sub>3</sub> van der waals heterostructure for 1.7v voltage all-inorganic perovskite solar cells, *Angew. Chem. Int. Ed.* 59 (2020) 21997–22001.
- [36] X. Zuo, B. Kim, B. Liu, D. He, L. Bai, W. Wang, C. Xu, Q. Song, C. Jia, Z. Zang, D. Lee, X. Li, J. Chen, Passivating buried interface via self-assembled novel sulfonium salt toward stable and efficient perovskite solar cells, *Chem. Eng. J.* 431 (2021), 133209.
- [37] J. Chen, N.-G. Park, Materials and methods for interface engineering towards stable and efficient perovskite solar cells, *ACS Energy Lett.* 5 (2020) 2742–2786.
- [38] H. Bi, B. Liu, D. He, L. Bai, W. Wang, Z. Zang, J. Chen, Interfacial defect passivation and stress release by multifunctional KPF<sub>6</sub> modification for planar perovskite solar cells with enhanced efficiency and stability, *Chem. Eng. J.* 418 (2021), 129375.
- [39] H. Bi, X. Zuo, B. Liu, D. He, L.e. Bai, W. Wang, X. Li, Z. Xiao, K. Sun, Q. Song, Z. Zang, J. Chen, Multifunctional organic ammonium salt-modified SnO<sub>2</sub> nanoparticles toward efficient and stable planar perovskite solar cells, *J. Mater. Chem. A* 9 (7) (2021) 3940–3951.
- [40] U. Bin Qasim, H. Bin Qasim, M.M. Saeed, M.H. Riaz, H. Imran, Investigating physical origin of dominant hysteresis phenomenon in perovskite solar cell, *J. Mater. Sci. Mater. Electronics* 32 (2021) 5274–5285.
- [41] M. Wang, Y. Lei, Y. Xu, L. Han, Z. Ci, Z. Jin, The J-V hysteresis behavior and solutions in perovskite solar cells, *Sol. RRL* 4 (12) (2020) 2000586.
- [42] W. Yao, S. Fang, Y. Wang, Z. Hu, L. Huang, X. Liu, T. Jiang, J. Zhang, J. Wang, Y. Zhu, Suppression of hysteresis in all-inorganic perovskite solar cells by the incorporation of PCBM, *Appl. Phys. Lett.* 118 (12) (2021) 123502.
- [43] X. Liu, Y. Zhang, L. Shi, Z. Liu, J. Huang, J.S. Yun, Y. Zeng, A. Pu, K. Sun, Z. Hameiri, J.A. Stride, J. Seidel, M.A. Green, X. Hao, Exploring inorganic binary alkaline halide to passivate defects in low-temperature-processed planar-structure hybrid perovskite solar cells, *Adv. Energy Mater.* 8 (2018) 1800138.
- [44] P. Zhu, S. Gu, X. Luo, Y. Gao, S. Li, J. Zhu, H. Tan, Simultaneous contact and grain-boundary passivation in planar perovskite solar cells using SnO<sub>2</sub>-KCl composite electron transport layer, *Adv. Energy Mater.* 10 (2019) 1903083.
- [45] D.-Y. Son, S.-G. Kim, J.-Y. Seo, S.-H. Lee, H. Shin, D. Lee, N.-G. Park, Universal approach toward hysteresis-free perovskite solar cell via defect engineering, *J. Am. Chem. Soc.* 140 (4) (2018) 1358–1364.
- [46] Y. Yang, J. Liang, Z. Zhang, C. Tian, X. Wu, Y. Zheng, Y. Huang, J. Wang, Z. Zhou, M. He, Z. Chen, C.-C. Chen, Suppressing residual lead iodide and defects in sequential-deposited perovskite solar cell via bidentate potassium dichloroacetate ligand, *ChemSusChem* n/a (2022).
- [47] F. Zheng, W. Chen, T. Bu, K.P. Ghiggino, F. Huang, Y. Cheng, P. Tapping, T.W. Kee, B. Jia, X. Wen, Triggering the passivation effect of potassium doping in mixed-cation mixed-halide perovskite by light illumination, *Adv. Energy Mater.* 9 (2019) 1901016.
- [48] Z. Tang, S. Uchida, T. Bessho, T. Kinoshita, H. Wang, F. Awai, R. Jono, M. Maitani, J. Nakazaki, T. Kubo, H. Segawa, Modulations of various alkali metal cations on organometal halide perovskites and their influence on photovoltaic performance, *Nano Energy* 45 (2018) 184–192.
- [49] P. Boonmongkolras, S.D.H. Naqvi, D. Kim, S.R. Pae, M.K. Kim, S. Ahn, B. Shin, Universal passivation strategy for the hole transport layer/perovskite interface via an alkali treatment for high-efficiency perovskite solar cells, *Sol. RRL* 5 (2021) 2000793.
- [50] S. Kandori, T. Oku, K. Nishi, T. Kishimoto, N. Ueoka, A. Suzuki, Fabrication and characterization of potassium- and formamidinium-added perovskite solar cells, *J. Ceram. Soc. Jpn.* 128 (10) (2020) 805–811.
- [51] M.F. Vildanova, A.B. Nikolskaia, S.S. Kozlov, O.K. Karyagina, O.I. Shevaleevskiy, Potassium doping effect on the photovoltaic performance of perovskite solar cells, *Tech. Phys. Lett.* 46 (3) (2020) 231–234.
- [52] Z. Zhou, X. Zou, J. Zhu, J. Cheng, H. Ren, C. Chang, Y. Yao, D. Chen, X. Yu, G. Li, J. Wang, B. Liu, K<sup>+</sup> doping effect on grain boundary passivation and photoelectronics properties of NiOx/perovskite films, *Chem. Phys. Lett.* 757 (2020), 137882.
- [53] Y. Huang, T. Liu, B. Wang, J. Li, D. Li, G. Wang, Q. Lian, A. Amini, S. Chen, C. Cheng, G. Xing, Antisolvent engineering to optimize grain crystallinity and hole-blocking capability of perovskite films for high-performance photovoltaics, *Adv. Mater.* 33 (38) (2021) 2102816.
- [54] S. Xiong, Z. Hou, S. Zou, X. Lu, J. Yang, T. Hao, Z. Zhou, J. Xu, Y. Zeng, W. Xiao, W. Dong, D. Li, X. Wang, Z. Hu, L. Sun, Y. Wu, X. Liu, L. Ding, Z. Sun, M. Fahlman, Q. Bao, Direct observation on p- to n-type transformation of perovskite surface region during defect passivation driving high photovoltaic efficiency, *Joule* 5 (2) (2021) 467–480.
- [55] F. Zhang, S. Ye, H. Zhang, F. Zhou, Y. Hao, H. Cai, J. Song, J. Qu, Comprehensive passivation strategy for achieving inverted perovskite solar cells with efficiency exceeding 23% by trap passivation and ion constraint, *Nano Energy* 89 (2021), 106370.

- [56] J. Chen, N.G. Park, Causes and solutions of recombination in perovskite solar cells, *Adv. Mater.* 31 (2019) 1803019.
- [57] Y. Huang, T. Liu, B. Wang, J. Li, D. Li, G. Wang, Q. Lian, A. Amini, S. Chen, C. Cheng, G. Xing, Antisolventengineering to optimize grain crystallinity and hole-blocking capability of perovskite films for high-performance photovoltaics, *Adv. Mater.* 33 (38) (2021) 2102816.
- [58] G. Kresse, J. Furthmüller, Efficiency of ab-initio total energy calculations for metals and semiconductors using a plane-wave basis set, *Comput. Mater. Sci.* 6 (1) (1996) 15–50.
- [59] G. Kresse, D. Joubert, From ultrasoft pseudopotentials to the projector augmented-wave method, *Phys. Rev. B* 59 (3) (1999) 1758–1775.
- [60] P.E. Blöchl, Projector augmented-wave method, *Phys. Rev. B* 50 (24) (1994) 17953–17979.
- [61] J.P. Perdew, K. Burke, M. Ernzerhof, Generalized gradient approximation made simple, *Phys. Rev. Lett.* 77 (18) (1996) 3865–3868.
- [62] M. Methfessel, A.T. Paxton, High-precision sampling for Brillouin-zone integration in metals, *Phys. Rev. B* 40 (6) (1989) 3616–3621.
- [63] J.D. Pack, H.J. Monkhorst, “Special points for Brillouin-zone integrations”—a reply, *Phys. Rev. B* 16 (4) (1977) 1748–1749.
- [64] S. Grimme, Semiempirical GGA-type density functional constructed with a long-range dispersion correction, *J. Comput. Chem.* 27 (15) (2006) 1787–1799.
- [65] S. Küfner, A. Schleife, B. Höffling, F. Bechstedt, Energetics and approximate quasiparticle electronic structure of low-index surfaces of SnO<sub>2</sub>, *Phys. Rev. B* 86 (2012), 075320.
- [66] K. Momma, F. Izumi, VESTA: a three-dimensional visualization system for electronic and structural analysis, *J. Appl. Crystallogr.* 41 (2008) 653–658.